iScience

CellPress
OPEN ACCESS

Article

Simultaneous photocatalytic biomass conversion and CO_2 reduction over high crystalline oxygen-doped carbon nitride

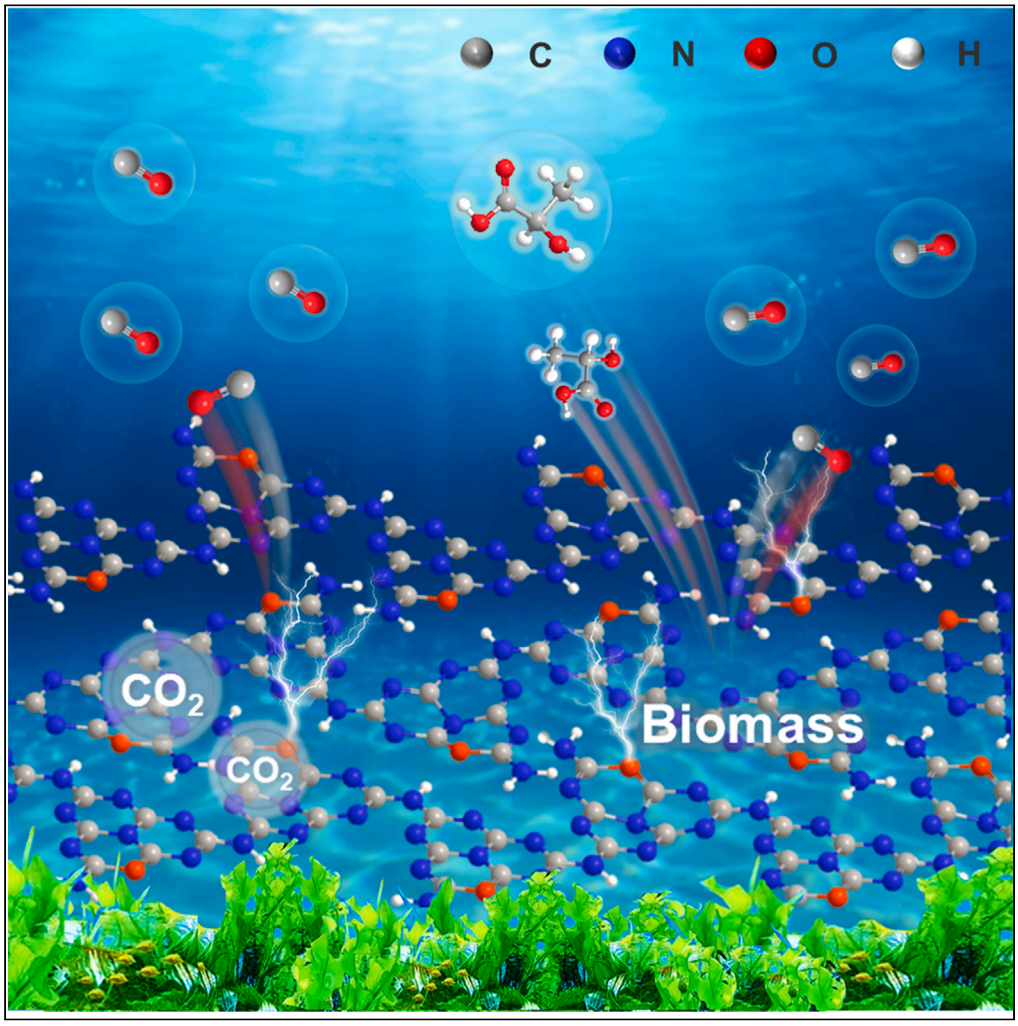

Zhendong Liu, Junqiang Zhang, Xinze Li, Rui Cui, Jiliang Ma, Runcang Sun

jlma@dlpu.edu.cn (J.M.)
rcsun3@dlpu.edu.cn (R.S.)

Highlights

Highly crystalline O-doped carbon nitride hollow nanotubes were designed

Boosted charge carriers separation by improved crystallinity and O-incorporated

Photocatalytic CO_2 reduction and biorefinery are achieved simultaneously

CO evolution rate over O-CNNTs-2.0 is 7.37 times higher than pure CN

Liu et al., iScience 26, 107416
August 18, 2023
https://doi.org/10.1016/j.isci.2023.107416

iScience

CellPress
OPEN ACCESS

Article

Simultaneous photocatalytic biomass conversion and CO_2 reduction over high crystalline oxygen-doped carbon nitride

Zhendong Liu,[1] Junqiang Zhang,[1] Xinze Li,[1] Rui Cui,[1] Jiliang Ma,[1,2,*] and Runcang Sun[1,*]

SUMMARY

Simultaneous photocatalytic biorefinery and CO_2 reduction to co-produce fuels and high value-added chemicals have recently attracted significant attention; however, comprehensive studies are still lacking. Herein, we report the preparation of highly crystalline oxygen-doped carbon nitride nanotubes (O-CNNTs-x) using an ammonium fluoride-assisted hydrothermal/calcination strategy. The hollow structure, high crystallinity, and O incorporation endowed the O-CNNTs-x with photocatalytic activity by considerably improving optical absorption and modulating the charge carrier motion. The lactic acid yield and CO evolution rate over O-CNNTs-2.0 reached 82.08% and 67.95 μmol g^{-1} h^{-1}, which are 1.57- and 7.37-fold times higher than those of CN, respectively. Moreover, ·OH plays a key role in the oxidation half-reaction. This study offers a facile approach for fabricating highly crystalline element-doped CN with a customizable morphology and electronic properties and demonstrates the viability of co-photocatalytic CO_2 reduction and biomass selective oxidation.

INTRODUCTION

Carbon dioxide (CO_2), primarily produced from the consumption of fossil fuels, poses two challenges, the energy crisis and the greenhouse effect.[1–3] Several approaches, such as electrocatalysis, thermal catalysis, and photocatalysis, have been developed for the conversion of CO_2.[4–6] Among them, photocatalytic reduction of CO_2 to valuable chemicals and fuels is a promising approach to alleviate the greenhouse effect and achieve 'carbon neutral' targets. However, the kinetics of the four-electron H_2O oxidation reaction is sluggish during this artificial photocatalytic CO_2 conversion, necessitating a large overpotential for O_2 evolution.[7–9] On the other hand, O_2 and H_2O can compete with the CO_2 reduction half-reaction in accepting electrons, leading to the generation of reactive oxygen species that can potentially damage the system.[9] These thermodynamic and kinetics limitations together result in low efficiency and poor selectivity for photocatalytic CO_2 transformation. In contrast, the photoreduction of CO_2 with sacrificial reagents (e.g., 1-benzyl-1,4-dihydronicotinamide, triethanolamine, and sodium sulfite) as the hole scavenger exhibits efficient accessibility for CO_2 conversion.[10–13] However, this approach still encounters certain limitations, such as the inefficiency of utilizing holes, the generation of redundant oxidation products, and an increase in overall system expenses.

Recently, photocatalytic selective oxidation of biomass to produce high value-added chemicals has aroused much attention.[14,15] A promising approach that has emerged is the integration of photocatalytic CO_2 reduction with biomass oxidation in a single reaction system, enabling the synergistic utilization of photogenerated electrons and holes while enhancing the value of the oxidation half-reaction.[16–19] As we know, to achieve this goal, catalysts play crucial roles. For instance, Reisner's group utilized a biohybrid photocatalyst, immobilizing formate dehydrogenase on TiO_2 to simultaneously generate formate through CO_2 reduction and oxidize cellulose.[17] This system produced up to 1.16 ± 0.04 $mmol_{formate}/g_{TiO2}$ in 24 h at 30°C and 101 kPa anaerobic conditions. Lam et al. reported the photocatalytic reduction of CO_2 to syngas and the selective oxidation of biomass-derived oxygenates or cellulose to formates using a hybrid photocatalyst consisting of a phosphonated cobalt bis(terpyridine) catalyst immobilized on TiO_2 powder.[18] The hybrid photocatalyst was repeatedly used and operated in aqueous solution at 25°C for several days to achieve a 17% cellulose to formate conversion. In these coupled reaction processes, biomass not only serves as a substitute for H_2O or hole scavengers to generate value-added chemicals, but also provides the reducing equivalents of protons and electrons to facilitate the activation/reduction of CO_2.[16] However, the utilized photocatalysts during these coupled reaction systems still faces challenges in terms of the high

[1]Liaoning Key Lab of Lignocellulose Chemistry and BioMaterials, Liaoning Collaborative Innovation Center for Lignocellulosic Biorefinery, College of Light Industry and Chemical Engineering, Dalian Polytechnic University, Dalian 116034, China

[2]Lead contact

*Correspondence: jlma@dlpu.edu.cn (J.M.), rcsun3@dlpu.edu.cn (R.S.)

https://doi.org/10.1016/j.isci.2023.107416

cost (e.g., formate dehydrogenase), low activity, and poor selectivity toward the target products. Furthermore, the aforementioned processes also suffered from long reaction time. Therefore, the design of an inexpensive, efficient, and highly selective photocatalyst for the coupled reaction system of biomass selective oxidation and CO_2 reduction is of great significance.

Polymeric carbon nitride (CN) is regarded as an attractive candidate for photocatalytic CO_2 reduction coupled with other oxidation half-reactions, due to its improved visible light response, ease of fabrication, and high chemical/thermal stability.[9,19–22] However, CN often faces inherent issues, such as sluggish charge mobility, rapid charge carrier recombination, and low crystallinity, resulting in limited photocatalytic activity.[23] Over the past decades, tremendous efforts have been dedicated to address these limitations through approaches like heterojunction construction,[24] morphology control,[25] defect engineering,[26] or heteroatom doping.[27] Among those approaches, heteroatom doping (e.g., P, B and O) is a commonly utilized method to regulate the electronic properties and enhance photocatalytic activities.[28–31] O-doping, in particular, has shown great promise as it forms coordination bonds with sp^2 hybridized C atoms, thereby modulating the intrinsic band gap structure of CN.[28,32] Meanwhile, O-doping can also accelerate carrier separation and enhance the capacity of visible light absorption.[28,32] Moreover, the preparation of O-doped CN is usually accompanied by morphology modulation that can further improve chemical, physical, and optical properties.[32–35] For instance, Du et al. prepared two-dimensional O-doped amorphous CN nanosheets using supercritical CO_2, demonstrating that partially substituting O for N in CN and two-dimensional structure improved optical/electronic properties and increased the specific surface area and active sites.[33] They achieved highly efficient photocatalytic degradation of methylene blue and CO_2 reduction.[33] Zhang et al. rationally designed O-doped CN nanotubes derived from supramolecular intermediates for photocatalytic water splitting.[35] The visible light absorption and charge separation of CN were improved by O doping. In addition, the hollow nanotube structure provides larger specific surface area and multiple diffuse reflections during the photocatalytic reaction, which can significantly contribute to the utilization of visible light.[35] These results suggest that O doping and morphology modulation are mutually reinforcing. However, it should be noted that the reported O-doped CN with morphology regulation in the literature mentioned above has relatively low crystallinity. It is known that low crystallinity in CN hinders charge transfer within the two-dimensional π-conjugated plane and increases the interlayer spacing, ultimately resulting in reduced photocatalytic activity.[36] Therefore, the exploration of a facile and efficient method to simultaneously achieve O doping, morphology modulation, and high crystallinity of CN is desirable yet challenging.

In this study, we have undertaken the rational design of highly crystalline CN nanotubes doped with O (O-CNNTs-x) using an ammonium fluoride-assisted hydrothermal/calcination approach. These nanotubes have the capability to simultaneously perform photocatalytic CO_2 reduction and selective oxidation of biomass. The incorporation of C-O bonds in the CN framework not only enhances its optical absorption capacity and charge separation efficiency, but also acts as a conduit for electron transfer, thereby increasing the catalytic activity. The unique spatial constraints provided by the hollow nanotube structure, along with its exceptional crystallinity, further contribute to its remarkable photocatalytic performance. In the case of O-CNNTs-2.0, the lactic acid yield reached 82.08%, and the CO evolution rate was measured at 67.95 $\mu mol\ g^{-1}\ h^{-1}$. These values were 1.57- and 7.37-fold higher, respectively, compared to those obtained with pure CN. To gain insights into the potential mechanism underlying the integration of photocatalytic biomass selective oxidation with CO_2 reduction, we conducted electron spin resonance (ESR), $^{13}CO_2$ isotope labeling experiments, and poisoning experiments. The outcomes of these experiments shed light on the fundamental understanding of the process. This study presents novel strategies for the co-photocatalytic selective oxidation of biomass and CO_2 reduction, offering new perspectives for the systematic development of highly crystalline photocatalytic materials with tailored morphology and electronic properties.

RESULTS AND DISCUSSION

Preparation and characterization of CN, O-CN and O-CNNTs-x

A series of O-CNNTs-x was preparation by a two-step strategy (Figure 1A). Briefly, the intermediates were first prepared via a fluorinated ammonia-assisted hydrothermal method and then calcined for 4 h in an N_2 atmosphere at 560°C to yield O-CNNTs-x. For comparison, bulk CN and O-CN were prepared. The morphology and microstructure of the obtained samples were evaluated by scanning electron microscopy (SEM) and transmission electron microscopy (TEM). As shown in Figures 1B and S1, O-CNNTs-2.0 is a

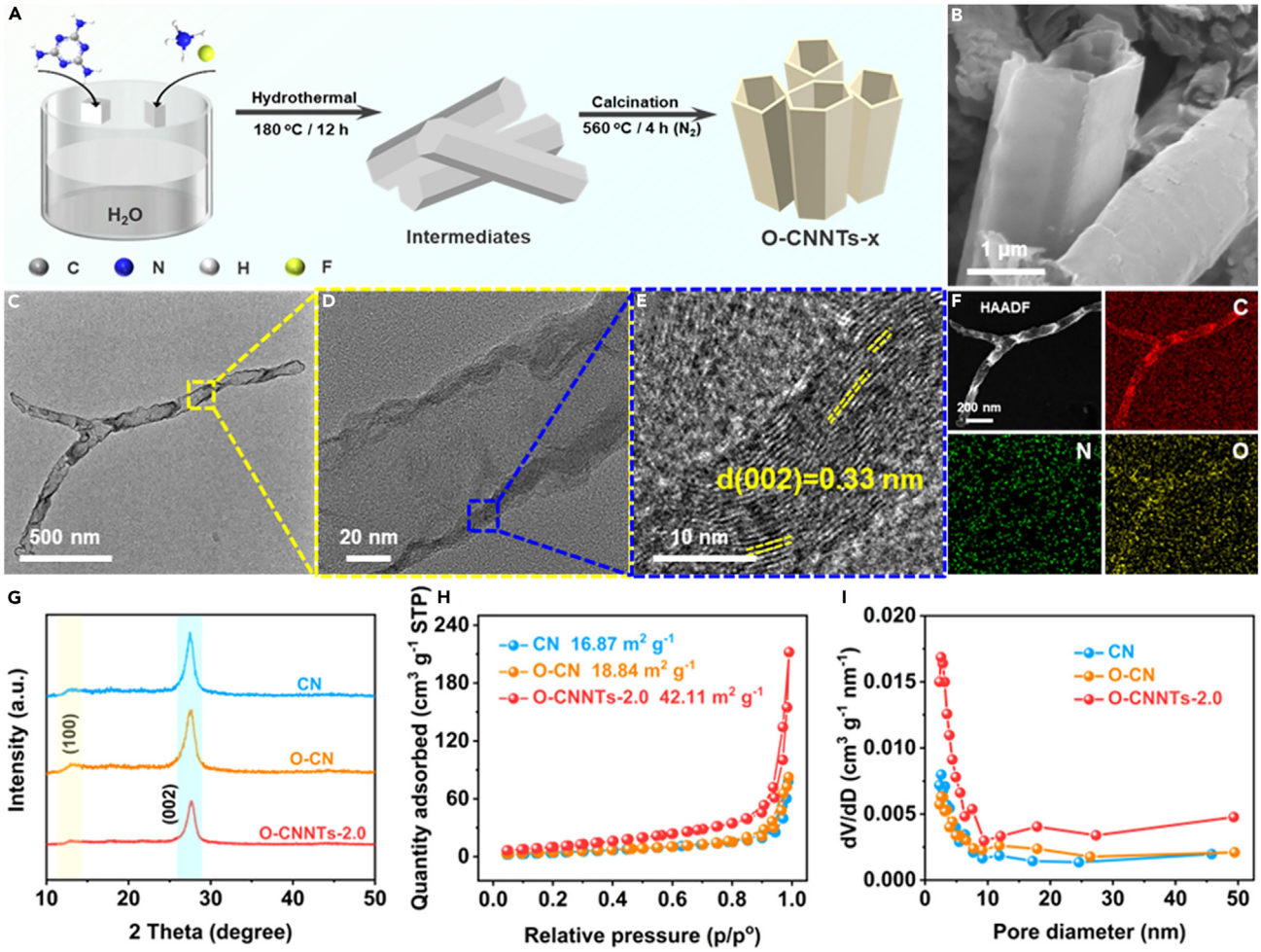

Figure 1. Preparation and morphology characterization of O-CNNTs-2.0

(A) Schematic illustration for the preparation of O-CNNTs-x photocatalysts.

(B) SEM image of O-CNNTs-2.0.

(C–F) TEM (C, D), HRTEM (E) and HAADF-STEM (F) images of O-CNNTs-2.0; (F) EDX mapping images of O-CNNTs-2.0.

(G) XRD patterns of CN, O-CN and O-CNNTs-2.0.

(H and I) N_2 adsorption/desorption isotherms (H) and the pore size distribution curves (I) of CN, O-CN and O-CNNTs-2.0.

nanotube-like structure, whereas CN and O-CN exhibit a typical nanosheet stacking structure. TEM images (Figures 1C and 1D) further confirm the hollow nanotube structure of O-CNNTs-2.0. In addition, the high-resolution TEM (HRTEM) image (Figure 1E) shows the crystalline nature of O-CNNTs-2.0 with a *d*-spacing of 0.33 nm, which belongs to the (002) lattice plane of CN.[37] The energy-dispersive X-ray spectroscopy (EDX) analysis (Figure 1F) shows that C, N, and O elements were observed and uniformly distributed on the surface of O-CNNTs-2.0, which confirms that O elements are successfully incorporated into the framework of CN.

X-ray diffraction (XRD) patterns of O-CNNTs-x, O-CN and CN are shown in Figures 1G and S2. O-CN and CN possess two characteristic peaks at 13.0° (100) and 27.3° (002), which belong to the in-plane repeating heptazine structure and the interlayer stacking of the conjugated aromatic system, respectively.[38] As compared with O-CN and CN, the main diffraction peak in the (002) crystal plane of O-CNNTs-x becomes weaker and slightly shifts from 27.5° to 27.3°, which suggests that the interlayer stacking distance of CN increases.[39] In addition, the diffraction peak of the (100) crystal plane can hardly be observed for O-CNNTs-3.0, which indicates that the connection pattern/microstructure of CN may have changed after O doping.[40] The specific surface area and pore structure were evaluated using N_2 adsorption/desorption isotherms and pore-size distribution curves. As depicted in Figure 1H, the CN, O-CN and O-CNNTs-2.0

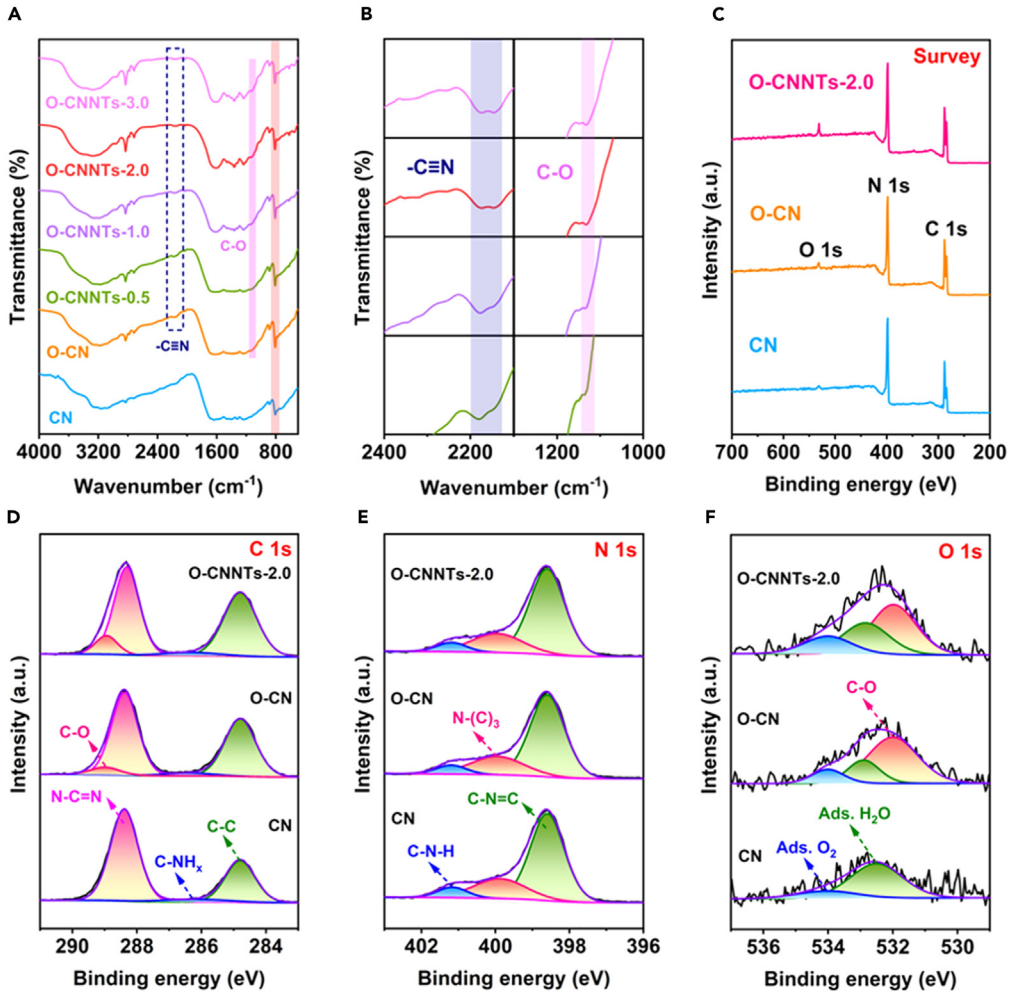

Figure 2. Component and chemical states of CN, O-CN and O-CNNTs-x

(A and B) (A) FT-IR spectra of CN, O-CN and O-CNNTs-x.

(B) FT-IR spectra of O-CNNTs-0.5, O-CNNTs-1.0, O-CNNTs-2.0, and O-CNNTs-3.0 with local magnification.

(C) XPS survey spectra of CN, O-CN and O-CNNTs-2.0.

(D–F) C 1s (D), N 1s (E) and O 1s (F) high-resolution XPS spectra of CN, O-CN and O-CNNTs-2.0.

exhibit type-IV isotherms, which indicates that the similar mesoporous structures.[41] Correspondingly, the pore sizes of all samples ranged from of 2–8 nm (Figure 1I). The calculated specific surface area of O-CN (18.84 $m^2\ g^{-1}$) is close to that of CN (16.87 $m^2\ g^{-1}$). In contrast, O-CNNTs-2.0 benefits from its hollow nanotube structure and has a specific surface area (42.11 $m^2\ g^{-1}$) that is nearly 2.5 times higher than that of CN. The significantly increased specific surface area implies that O-CNNTs-2.0 can provide sufficient charge-transfer channels and more catalytic active sites to facilitate photocatalytic redox reactions.[41,42]

Fourier transform infrared spectroscopy (FT-IR) was performed to characterize the structures of CN, O-CN and O-CNNTs-x. In the FT-IR spectra of O-CNNTs-x, O-CN and CN (Figures 2A and 2B), the peak at 3000-3500 cm^{-1} arises from the N-H or the O-H stretching mode, whereas the fingerprint signals between 1200 and 1600 cm^{-1} are related to the stretching and bending vibrations of the conjugated CN heterocyclic ring. The strong peak at 809 cm^{-1} originates from the out-of-plane bending of the heptazine rings.[39,43] Furthermore, two new peaks appear at 2178 and 2157 cm^{-1} in O-CNNTs-x are attributed to the asymmetric stretching modes of cyano group (-C≡N) that are came from the terminal amino group in the melon structural unit.[44] Meanwhile, the formation of C-O bonds in O-CNNTs-x is identified by the band at 1150 cm^{-1}.[38] X-ray photoelectron spectroscopy (XPS) measurements were performed to reveal the atomic environment and chemical states of the samples. XPS survey spectrum (Figure 2C) of O-CNNTs-2.0 exhibits obvious C 1s,

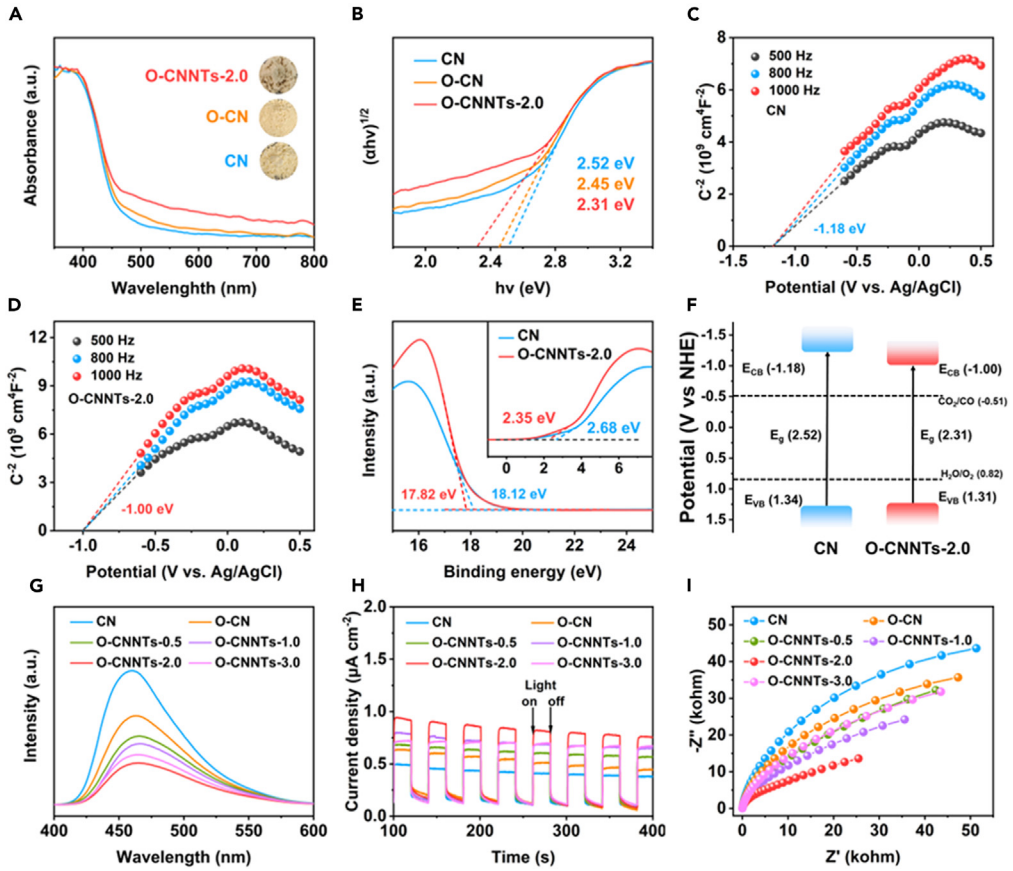

Figure 3. Characterization of the photo-electro properties of catalysts

(A and B) UV-vis DRS spectra (A) and Kubelka–Munk plots (B) of CN, O-CN, and O-CNNTs-2.0.

(C–F) M-S plots (C, D), UPS (E) and the related band structure scheme (F) of corresponding samples.

(G–I) PL emission spectra (G), transient photocurrent curves (H) and EIS (I) of CN, O-CN, and O-CNNTs-x.

N 1s and O 1s signals. Meanwhile, the elemental O content of O-CNNTs-2.0 increased to 4.8 at%, which is higher than that of CN (Table S1). For the C 1s XPS spectra (Figure 2D), three peaks at 284.8, 286.3, and 288.4 eV can be identified owing to the presence of C atoms in the graphite carbon (C-C/C=C), C-NH_x, and aromatic N-C=N units.[41] Meanwhile, a new peak located at 288.9 eV, which is related to C-O bonds, can be observed in O-CN and O-CNNTs-2.0. As shown in the N 1s spectra (Figure 2E), all samples display three peaks at 398.6, 399.9, and 401.2 eV, corresponding to C-N=C, N-$(C)_3$ and C-N-H groups, respectively.[9] For the O 1s XPS spectra (Figure 2F) of O-CN and O-CNNTs-2.0, three peaks at 534.0, 532.8, and 532.0 eV are attributed to the adsorbed water, adsorbed oxygen, and C-O bond, respectively.[39,41]

The effects of hollow nanotube structures, high crystallinity and C-O bonds on the optical properties, and energy band structure of CN were systematically analyzed. Figures 3A and S3 show the UV-vis diffuse reflectance spectra (UV-vis DRS) of O-CNNTs-x, O-CN, and CN. The absorption edge of O-CNNTs-x has a slight red shift as compared with those of CN and O-CN. According to the Kubelka–Munk function,[26,45] the bandgaps (E_g) of CN, O-CN, O-CNNTs-0.5, O-CNNTs-1.0, O-CNNTs-2.0 and O-CNNTs-3.0 were determined to be 2.52, 2.45, 2.40, 2.38, 2.31, and 2.25 eV, respectively (Figures 3B and S4). These results indicate that high crystallinity, hollow nanotube structures and introduction of C-O bonds can improve the light absorption and narrow the E_g of CN. Subsequently, Mott-Schottky (M-S) plots and ultraviolet photoelectron spectroscopy (UPS) of CN and O-CNNTs-2.0 were also implemented to identify the details of their band positions. Figures 3C and 3D show that both CN and O-CNNTs-2.0 are n-type semiconductors owing to their positive slopes of the M-S curve.[28] Furthermore, the flat-band potentials (E_{FB}) of CN and O-CNNTs-2.0 are estimated to be −1.18 and −1.00 V (vs. Ag/AgCl), respectively. Then, the E_{FB} of CN and O-CNNTs-2.0 can be converted to −0.98 and −0.80 V (vs. normal hydrogen electrode (NHE.)),

respectively, by the Nernst equation ($E_{NHE.} = E_{Ag/AgCl} + 0.197$, pH = 7). Due to the conduction band position (E_{CB}) of n-type semiconductors is usually 0.2 V lower than the E_{FB}, the E_{CB} values of CN and O-CNNTs-2.0 are −1.18 and −1.00 V (vs. NHE.), respectively.[28,46] Moreover, the valence band positions (E_{VB}) and work function (Φ) of CN and O-CNNTs-2.0 are confirmed using UPS analysis. Figure 3E shows that the onset energies (E_{onset}) of CN and O-CNNTs-2.0 are 2.68 and 2.35 eV, and their cutoff energies (E_{cutoff}) are 18.12 and 17.82 eV, respectively. Therefore, the E_{VB} values of CN and O-CNNTs-2.0 are calculated to be 5.78 and 5.75 eV using the formula: $E_{VB} = 21.22 - (E_{cutoff} - E_{onset})$, respectively, where 21.22 is the UV excitation energy.[47,48] According to the reference standard that 0 V versus reversible hydrogen electrode is equal to −4.44 eV, the E_{VB} values of CN and O-CNNTs-2.0 are 1.34 eV (5.78 - 4.44 eV) and 1.31 eV (5.75 - 4.44 eV), respectively. Furthermore, the Φ of CN and O-CNNTs-2.0 are computed to be 3.10 and 3.40 eV, respectively ($\Phi = 21.22 - E_{cutoff}$).[49] The schematic band structure diagrams of CN and O-CNNTs-2.0 are shown in Figure 3F based on the abovementioned discussion.

The photoinduced charge separation efficiency of CN, O-CN and O-CNNTs-x was monitored by the steady-state photoluminescence (PL) emission spectra. As shown in Figure 3G, the PL emission peak of O-CNNTs-x is significantly lower than those of CN and O-CN, especially for O-CNNTs-2.0, which indicates the restrained recombination rate of photogenerated carriers. This result may be attributed to the formation of an internal electric field to facilitate the separation of electron-hole (e^--h^+) pairs caused by lattice strain, changes in the C-N bond length and electron polarization effects.[50,51] To gain further insights into the charge behavior, the transient photocurrent response and electrochemical impedance spectra (EIS) of all samples were also recorded. As shown in Figure 3H, the photocurrent density of O-CNNTs-x is higher than those of CN and O-CN, where the photocurrent density of O-CNNTs-2.0 is about 2.4 times that of CN, which indicates efficient photogenerated charge separation in O-CNNTs-x.[45] Figure 3I shows that the arc radii of O-CNNTs-x in the EIS are also smaller than those of CN and O-CN, with O-CNNTs-2.0 exhibiting the smallest arc radii, suggesting easier separation/transfer of photogenerated e^--h^+ pairs in O-CNNTs-x.[41] These results indicate that the presence of highly crystalline ordered structures and hollow nanotube structures as well as the introduction of C-O bonds greatly enhance the charge carrier separation/migration dynamics of O-CNNTs-x.

Photocatalyst activity tests

A series of tests was conducted to understand the role of pH on the photocatalytic reduction of CO_2 coupled with selectivity oxidation of xylose. As shown in Table S2 (entry 1), a 61.05% yield of lactic acid and 154.49 μmol g^{-1} of CO were obtained at 30°C for 5 h by irradiation with 10 W visible light using O-CNNTs-2.0 (20 mg), KOH solution (30 mL, 1.0 M), xylose (100 mg), and CO_2 (110 kPa). Notably, by replacing the KOH solution (1.0 M) with the HCl solution (1.0 M) or H_2O, the photocatalytic performance is completely suppressed and only trace amounts of lactic acid and CO are produced (Table S2, entries 2–3). This result suggests that alkalinity favors the co-photocatalysis of xylose selective oxidation and CO_2 reduction.[52] Moreover, comparative experiments were conducted using Ar instead of CO_2 to examine the source of the generated CO. Table S2 (entry 4) shows that 92.43 μmol g^{-1} of CO is produced. Thus, the CO in the product is derived from the CO_2 reduction and the selective oxidation of xylose. Moreover, the production of lactic acid increased from 61.05% to 67.85%, which is in line with our previous report.[19,52] Subsequently, the $^{13}CO_2$ isotope labeling experiments of O-CNNTs-2.0 were performed to further identify and trace the origins of the generated CO. As displayed in Figure 4A, the two peaks at m/z = 28 and 29 were assigned to ^{12}CO and ^{13}CO, respectively, suggesting that part of CO came from CO_2. These results confirm the feasibility of co-photocatalytic biomass refining and CO_2 reduction. Furthermore, only a 9.85% yield of lactic acid and 1.72 μmol g^{-1} of CO were detected under dark conditions (Table S2, entry 5), which indicates the importance of light in the selective oxidation of xylose coupled with the CO_2 reduction. For the control experiment without adding xylose, no CO product was obtained, suggesting that the xylose was essential to drive the CO_2 reduction reaction (Table S2, entry 6). The photocatalytic performance of selective oxidation of biomass coupled with CO_2 reduction on CN, O-CN and O-CNNTs-x was investigated. Figure 4B shows that the optimal CO production rate of 154.49 μmol g^{-1} is recorded for O-CNNTs-2.0, which is 7.37- and 4.46-fold higher than CN of 20.97 μmol g^{-1} and O-CN of 34.64 μmol g^{-1}, respectively. Correspondingly, the yields of lactic acid were 38.91%, 44.00%, 46.11%, 50.29%, 61.05%, and 49.01% in the CN, O-CN, O-CNNTs-0.5, O-CNNTs-1.0, O-CNNTs-2.0, and O-CNNTs-3.0, respectively. As shown in Figure S5A, small amounts of by-products (e.g., formic acid, glyceraldehyde) were also detected. In addition, the lactic acid selectivity of O-CN was 60.32%, which is higher than that of CN (55.07%). Meanwhile, morphology control, increased crystallinity and introduction of C-O bonds in O-CNNTs-2.0 were effective

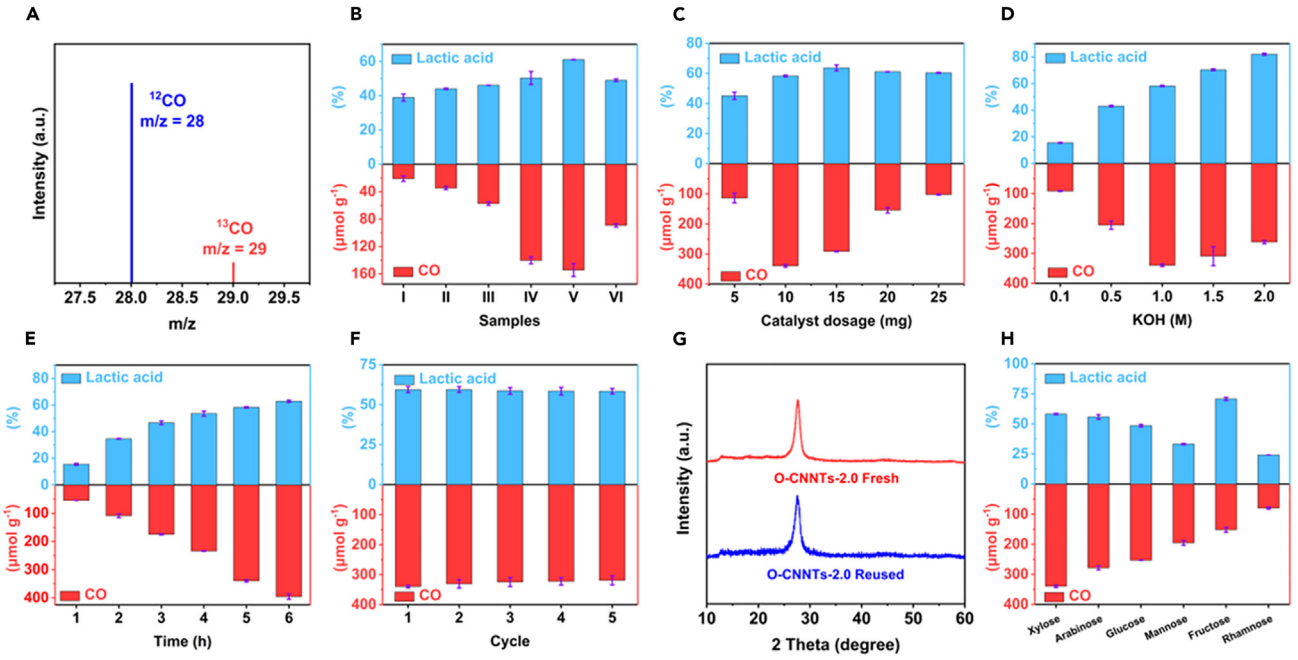

Figure 4. Photocatalytic biomass refining coupled with CO_2 reduction

(A) MS spectrum of the CO generated from the $^{13}CO_2$ isotope experiments.

(B) Photocatalytic CO evolution and lactic acid synthesis using 20 mg of catalyst (I: CN, II: O-CN, III: O-CNNTs-0.5, IV: O-CNNTs-1.0, V: O-CNNTs-2.0, VI: O-CNNTs-3.0) with xylose (100 mg) in 30.0 mL of KOH solution (1.0 M) for 5 h.

(C) Photocatalytic CO evolution and lactic acid synthesis using xylose (100 mg) with different O-CNNTs-2.0 dosage in 30.0 mL of KOH solution (1.0 M) for 5 h.

(D) Photocatalytic CO evolution and lactic acid synthesis using O-CNNTs-2.0 (10 mg) and xylose (100 mg) in 30.0 mL of KOH solution with different concentrations for 5 h.

(E) Photocatalytic CO evolution and lactic acid synthesis using O-CNNTs-2.0 (10 mg) with xylose (100 mg) in 30.0 mL of KOH solution (1.0 M).

(F) Recycling of O-CNNTs-2.0.

(G) XRD patterns of the fresh and reused O-CNNTs-2.0 photocatalysts.

(H) The selective oxidation of different biomass-derived monosaccharides to lactic acid coupled with CO_2 reduction photocatalyzed by O-CNNTs-2.0.

in improving the selectivity of the product, resulting in a significant increase in lactic acid selectivity to 79.02%.

The catalyst dosage is an important influence on the photocatalytic reaction. Excessive catalyst dosage may impede the transmission and absorbance of light, while low catalyst dosage may affect the photocatalytic efficiency due to the insufficient catalytic sites.[28,53] As shown in Figure 4C, the best CO production rate (339.75 μmol g^{-1}) can be obtained at a photocatalyst dosage of 10 mg. When the O-CNNTs-2.0 dosage exceeds 10 mg, the CO production rate is severely weakened. For lactic acid, as the photocatalyst dosage increased from 5 to 25 mg, the yield initially demonstrated an ascending trend but eventually plateaued. The optimal lactic acid yield of 63.65% was recorded for the O-CNNTs-2.0 reaction system of 15 mg. Figure S5B shows that variations in catalyst dosage had less effect on formic acid yield, glyceraldehyde yield, lactic acid selectivity, and xylose conversion. Based on the analysis presented in Figures 4C and S5B, 10 mg of O-CNNTs-2.0 was used in the following tests. Furthermore, pH plays a crucial role in the oxidation of xylose to biomass-derived organic acids. According to previous reports,[19,52] high alkali concentrations increase the production of lactic acid, while low alkali concentrations facilitate the generation of xylonic acid. As shown in Figure 4D, as the KOH concentration raised from 0.1 to 2.0 M, the yield of lactic acid continuously increased. Meanwhile, the evolution rate of CO greatly increased to a high level and then decreased when the KOH concentration was increased from 0.1 to 2.0 M, with the optimal evolution rate of 339.75 μmol g^{-1} reached at 1.0 M KOH. The solubility of CO_2 is positively correlated with the concentration of KOH, resulting in increased CO_2 dissolved on the photocatalyst surface and ultimately enhancing the efficiency of CO_2 reduction. However, in systems exhibiting exceedingly high alkalinity, the surface adsorbed protons face challenges in binding to the adsorbed $*CO_2$, impeding reduction of CO_2.[54] Alternatively, this phenomenon may be attributed to the increased selectivity of lactic acid under high alkalinity

conditions, resulting in a potential limitation in the availability of CO sources (glyceraldehyde) through the isomerization of dihydroxyacetone.[55] The hypothesis is supported by the increasing lactic acid yield/selectivity observed in Figures 4D and S5C as alkalinity increases. As shown in Figure 4E, the irradiation time had a great influence on the co-photocatalysis of xylose selective oxidation and CO_2 reduction. With the extension of the irradiation time, the yield of lactic acid initially increased and subsequently reached a plateau, probably owing to the complete consumption of xylose resulting in the further participation of the produced lactic acid in the reduction of CO_2 as a sacrificial agent.[56,57] Clearly, the CO production rate linearly increased with increasing illumination time, reaching a maximum (395.85 μmol g^{-1}) at 6 h. Of note, the extended illumination time resulted in a significant increase in xylose conversion and lactic acid selectivity (Figure S5D).

The recycling and universality tests

The cyclability of O-CNNTs-2.0 was investigated. As shown in Figure 4F, the lactic acid yields/CO evolution rates were 59.44%/339.75 μmol g^{-1}, 59.47%/330.80 μmol g^{-1}, 58.66%/324.59 μmol g^{-1}, 58.47%/322.30 μmol g^{-1}, and 58.39%/319.11 μmol g^{-1} in the 1st, 2nd, 3rd, 4th, and 5th cycles, respectively. Obviously, only a slight change in lactic acid yield and CO generation rate was observed after five cycles of recycling tests. Furthermore, no obvious changes were observed for the fresh and reused O-CNNTs-2.0 through TEM and XRD characterizations (Figures 4G and S5E). All the results indicated that the O-CNNTs-2.0 has robust stability. Moreover, a series of typical biomass-derived monosaccharides was screened to assess the universality of O-CNNTs-2.0. As shown in Figure 4H, the yields of lactic acid and the generation rates of CO were 24.10%/79.50 μmol g^{-1} (rhamnose), 70.75%/151.75 μmol g^{-1} (fructose), 33.2%/195.07 μmol g^{-1} (mannose), 48.48%/253.04 μmol g^{-1} (glucose), 55.79%/278.52 μmol g^{-1} (arabinose), and 59.44%/339.75 μmol g^{-1} (xylose), respectively. Overall, O-CNNTs-2.0 is an efficient catalyst to drive the co-photocatalysis of selectivity oxidation of biomass-derived monosaccharides and CO_2 conversion.

The effects of different oxidation active species on biomass refining and CO_2 reduction

To detect the active species produced during the photocatalysis process, ESR characterization was performed. In general, 2,2,6,6-tetramethylpiperidine-*N*-oxyl (TEMPO) was used as the spin-trapping agent to trap e^- and h^+, whereas hydroxyl radicals (·OH) were captured by 5,5-dimethyl-1-pyrroline-*N*-oxide (DMPO).[28,47,58] Figure 5A shows that triple TEMPO signals with intensities of 1:1:1 can be observed under dark conditions in the CN or O-CNNTs-2.0 system. Instead, the gradual flattening of the ESR signals was observed after illuminating the O-CNNTs-2.0 or CN system for 5 min with visible light, which was caused by TEMPO in the system being reduced to hydroxylamine (TEMPOH) by capturing photogenerated e^-. After 10 min of visible light irradiation, the TEMPO signal peak intensity in the O-CNNTs-2.0 system was lower than that in the CN system (Figure S6A), which indicates that more e^- were generated.[57] Therefore, the efficient separation of e^--h^+ pairs make O-CNNTs-2.0 active in the co-photocatalysis of CO_2 conversion and biorefinery. Furthermore, the emergence of e^- and h^+ occurs invariably in pairs, indicating that the trend observed in the ESR spectra of h^+ is analogous to that of e^- (Figures 5B and S6B).[28] DMPO can be used to form DMPO-·OH adducts after capturing ·OH, and the corresponding signals can be detected by ESR. As shown in Figure 5C, no signals of DMPO-·OH adducts were detected in the absence of visible light, suggesting that ·OH generation does not occur in the dark. In addition, DMPO-·OH signals with an intensity of 1:2:2:1 can be found in the O-CNNTs-2.0 or CN system under visible-light irradiation, and increased with longer irradiation time (Figures 5C and S6C). Moreover, DMPO-·OH adduct signals were stronger in the O-CNNTs-2.0 system than in the CN system, implying that more ·OH was produced.[57] Poisoning experiments in Figure 5D reveal the direct impact of the abovementioned oxidation active species on the photocatalytic oxidation process. Of note, the addition of *p*-phthalic acid (PTA, for ·OH) and ethylenediaminetetraacetic acid (EDTA, for h^+) into the reaction system resulted in a significant decrease in the yield of lactic acid, dropping from 58.21% to 28.21% and 23.09%, respectively. These results demonstrated that ·OH and h^+ facilitated the photocatalytic selective oxidation of xylose.

Possible reaction pathways of simultaneous CO_2 photoreduction and xylose photooxidation via O-CNNTs-2.0

According to previous reports[14,15,46,59–62] and the abovementioned analysis, we propose a possible mechanism for the simultaneous selective oxidation of xylose coupled with CO_2 reduction on O-CNNTs-2.0, as illustrated in Figure 6. Under visible light irradiation, O-CNNTs-2.0 generates photoexcited e^- and h^+. The e^- in CB react with absorbed CO_2 to form a COOH* intermediate. CO is subsequently produced from the COOH* intermediates through proton and e^- transfer, as well as dehydration processes.[46,59] On the other

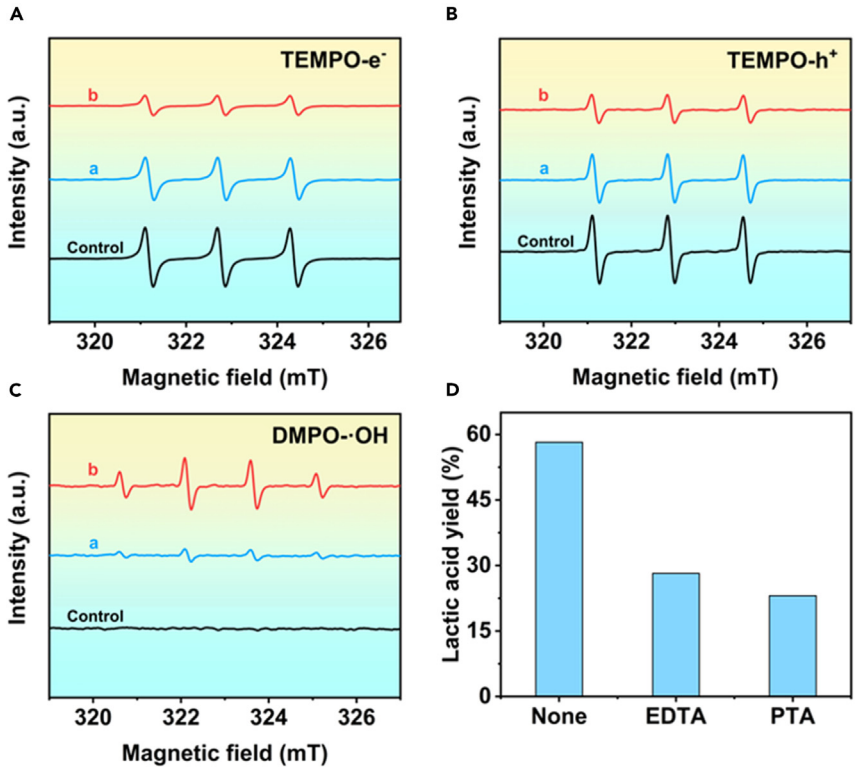

Figure 5. Investigation of the active species

(A–C) TEMPO ESR spin-labelling for e^- (A) and h^+ (B), DMPO ESR spin-labelling for ·OH (C), (Control: in the dark conditions with photocatalyst or irradiation without photocatalyst; a and b represent CN and O-CNNTs-2.0).

(D) The effects of different oxidation active species on the synthesis of lactic acid.

hand, the h^+ generated in the VB participate in the formation of oxidation active species and the conversion of xylose. The presence and impact of h^+/·OH on the oxidation of xylose were confirmed through ESR and poisoning tests. Specifically, xylose undergoes isomerization to xylulose.[14] Then, the C3-C4 bond of xylulose is cleaved via retro-aldol condensation, resulting in 1,3-dihydroxyacetone and glycolaldehyde.[14,60] After dehydration, 1,3-dihydroxyacetone is transformed into pyruvaldehyde. Subsequently, pyruvaldehyde undergoes intermolecular Cannizzaro reaction to produce lactic acid.[14] Another pathway for lactic acid synthesis involves aldol condensation of glycolaldehyde to generate erythrose.[59] Then, through dehydration and isomerization from erythrose, 2-carbonyl-4-hydroxybutyraldehyde is formed, which further decomposes into formic acid and pyruvaldehyde via retro-aldol condensation.[15,60] Lactic acid is finally produced through the intermolecular Cannizzaro reaction of pyruvaldehyde.[60] Additionally, CO can also be obtained from the further decomposition of formic acid and glyceraldehyde.[61,62]

Conclusions

In summary, we first presented a photocatalytic redox system for photocatalytic CO_2 reduction coupled with biomass selective oxidation to co-produce CO and lactic acid using O-CNNTs-x. Here, the O-CNNTs-x was prepared via an ammonium fluoride-assisted hydrothermal/calcination strategy. The incorporation of C-O bonds in CN enhances the optical absorption capacity and charge separation efficiency and serves as an e^--transfer conduit to expedite e^- transfer, thereby elevating the photocatalytic activity (CO evolution rate: 67.95 μmol g^{-1} h^{-1}; lactic acid yield: 82.08%). The unique spatial confinement in hollow nanotubes (O-CNNTs-2.0) coupled with high crystallinity also helped improve its performance. In addition, O-CNNTs-2.0 not only shows favorable stability and reusability after five cycles, but also maintains high lactic acid and CO production when replacing xylose with other biomass-derived monosaccharides (e.g., rhamnose, fructose, mannose, glucose, arabinose). ESR and poisoning experiments revealed that ·OH plays a crucial role in promoting the biomass photooxidation, while the $^{13}CO_2$ isotope labeling experiments demonstrated that part of CO was derived from biomass selective oxidation. This work offers

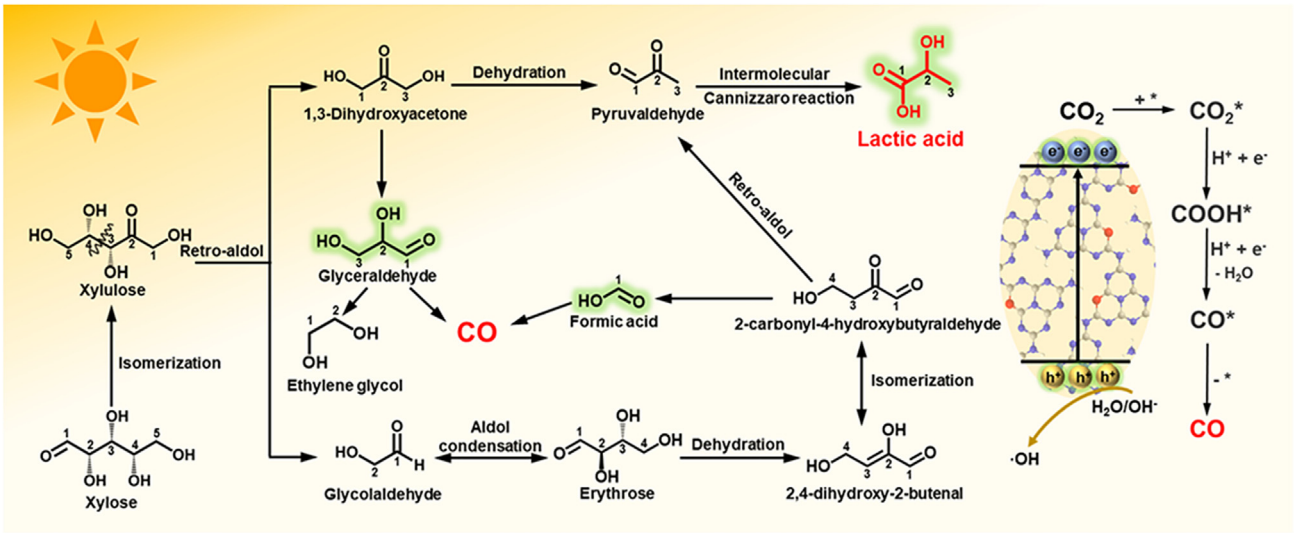

Figure 6. Proposed reaction mechanism

Possible reaction pathways of simultaneous CO_2 photoreduction and xylose photooxidation via O-CNNTs-2.0.

new insights into the rational design of highly crystalline element-doped catalysts with morphology tailoring and the efficient use of photogenerated e^- and h^+ for the co-designing of biomass selective oxidation and CO_2 reduction reaction pathways.

Limitations of the study

This study demonstrated the feasibility of highly crystalline oxygen-doped CN nanotubes for photocatalytic biomass refining coupled with CO_2 reduction. Experimental results indicated that the photocatalysts had good xylose/CO_2 conversion and excellent lactic acid selectivity as well as considerable CO generation. However, the in-depth understanding of the photocatalytic mechanism, in particular the exact role of photogenerated e^- and h^+ during xylose oxidation and CO_2 reduction, is still needed through further *in situ* characterization and density functional theory (DFT) calculations. We will continue our research on related projects using more advanced technologies to better appreciate the in-depth mechanisms.

STAR★METHODS

Detailed methods are provided in the online version of this paper and include the following:

- KEY RESOURCES TABLE
- RESOURCE AVAILABILITY
  - Lead contact
  - Materials availability
  - Data and code availability
- METHOD DETAILS
  - Preparation of O-CNNTs-x, O-CN, and CN
  - Photocatalytic activity tests
  - Poisoning experiments and universality tests
  - Cyclic experiments
  - Isotope-labelling testing
  - Catalyst characterization
  - Photoelectrochemical measurements
  - Products analysis
- QUANTIFICATION AND STATISTICAL ANALYSIS

SUPPLEMENTAL INFORMATION

Supplemental information can be found online at https://doi.org/10.1016/j.isci.2023.107416.

ACKNOWLEDGMENTS

This work was supported by the Foundation of NSFC-CONICFT Joint Project (No. 51961125207), National Natural Science Foundation of China (22008018), Dalian Outstanding Young Scientific and Technological Talents (2022RY24), China Postdoctoral Science Foundation (2020M670716), the Foundation of Guangxi Key Laboratory of Clean Pulp & Papermaking and Pollution Control (No. 2021KF08), the College of Light Industry and Food Engineering, Guangxi University. The authors also thank the Shiyanjia Lab (https://www.shiyanjia.com) for XPS analysis.

AUTHOR CONTRIBUTIONS

Z.L.: Conceptualization, Methodology, Investigation, Data curation, Writing - original draft, Visualization. **J.Z.**: Validation, Writing - review and editing. **X.L.**: Validation. **R.C.**: Validation. **J.M.**: Conceptualization, Investigation, Project administration, Methodology, Supervision, Writing – review and editing, Funding acquisition. **R.S.**: Resources, Investigation, Project administration, Supervision, Writing – review and editing.

DECLARATION OF INTERESTS

The authors declare no competing interests.

Received: May 14, 2023
Revised: June 26, 2023
Accepted: July 14, 2023
Published: July 19, 2023

REFERENCES

1. Lashof, D.A., and Ahuja, D.R. (1990). Relative contributions of greenhouse gas emissions to global warming. Nature *344*, 529–531. https://doi.org/10.1038/344529a0.

2. Kaufman, D.S., and Broadman, E. (2023). Revisiting the holocene global temperature conundrum. Nature *614*, 425–435. https://doi.org/10.1038/s41586-022-05536-w.

3. Turner, J.M. (2022). The matter of a clean energy future. Science *376*, 1361. https://doi.org/10.1126/science.add5094.

4. Das, S., Pérez-Ramírez, J., Gong, J., Dewangan, N., Hidajat, K., Gates, B.C., and Kawi, S. (2020). Core-shell structured catalysts for thermocatalytic, photocatalytic, and electrocatalytic conversion of CO_2. Chem. Soc. Rev. *49*, 2937–3004. https://doi.org/10.1039/C9CS00713J.

5. Liang, J., Yu, H., Shi, J., Li, B., Wu, L., and Wang, M. (2023). Dislocated bilayer MOF enables high-selectivity photocatalytic reduction of CO_2 to CO. Adv. Mater. *35*, 2209814. https://doi.org/10.1002/adma.202209814.

6. Lai, W., Qiao, Y., Zhang, J., Lin, Z., and Huang, H. (2022). Design strategies for markedly enhancing energy efficiency in the electrocatalytic CO_2 reduction reaction. Energy Environ. Sci. *15*, 3603–3629. https://doi.org/10.1039/D2EE00472K.

7. An, X., Tang, Q., Lan, H., Liu, H., Yu, X., Qu, J., Lin, H., and Ye, J. (2022). Facilitating molecular activation and proton feeding by dual active sites on polymeric carbon nitride for efficient CO_2 photoreduction. Angew. Chem. Int. Ed. *61*, e202212706. https://doi.org/10.1002/anie.202212706.

8. Zhou, J., Li, J., Kan, L., Zhang, L., Huang, Q., Yan, Y., Chen, Y., Liu, J., Li, S.-L., and Lan, Y.-Q. (2022). Linking oxidative and reductive clusters to prepare crystalline porous catalysts for photocatalytic CO_2 reduction with H_2O. Nat. Commun. *13*, 4681. https://doi.org/10.1038/s41467-022-32449-z.

9. Liu, Q., Lin, J., Cheng, H., Wei, L., and Wang, F. (2023). Simultaneous co-photocatalytic CO_2 reduction and ethanol oxidation towards synergistic acetaldehyde synthesis. Angew. Chem. Int. Ed. *62*, e202218720. https://doi.org/10.1002/anie.202218720.

10. Zhao, F., Feng, Y., Wang, Y., Zhang, X., Liang, X., Li, Z., Zhang, F., Wang, T., Gong, J., and Feng, W. (2020). Two-dimensional gersiloxenes with tunable bandgap for photocatalytic H_2 evolution and CO_2 photoreduction to CO. Nat. Commun. *11*, 1443. https://doi.org/10.1038/s41467-020-15262-4.

11. An, D., Nishioka, S., Yasuda, S., Kanazawa, T., Kamakura, Y., Yokoi, T., Nozawa, S., and Maeda, K. (2022). Alumina-supported alpha-iron(III) oxyhydroxide as a recyclable solid catalyst for CO_2 photoreduction under visible light. Angew. Chem. Int. Ed. *61*, e202204948. https://doi.org/10.1002/anie.202204948.

12. Barman, S., Singh, A., Rahimi, F.A., and Maji, T.K. (2021). Metal-free catalysis: A redox-active donor-acceptor conjugated microporous polymer for selective visible-light-driven CO_2 reduction to CH_4. J. Am. Chem. Soc. *143*, 16284–16292. https://doi.org/10.1021/jacs.1c07916.

13. Müller, A.V., Faustino, L.A., de Oliveira, K.T., Patrocinio, A.O.T., and Polo, A.S. (2023). Visible-light-driven photocatalytic CO_2 reduction by Re(I) photocatalysts with N-heterocyclic substituents. ACS Catal. *13*, 633–646. https://doi.org/10.1021/acscatal.2c05521.

14. Zhong, M., Li, X., Chu, X., Gui, H., Zuo, S., Yao, C., Li, Z., and Chen, Y. (2022). Solar driven catalytic conversion of cellulose biomass into lactic acid over copper reconstructed natural mineral. Appl. Catal. B Environ. *317*, 121718. https://doi.org/10.1016/j.apcatb.2022.121718.

15. Liu, K., Liu, Z., Yao, S., Sun, S., Ma, J., and Sun, R. (2022). $CuInS_2$ quantum dots anchored onto the three-dimensional flexible self-supporting graphene oxide array with regulatable crystallinity and defect density for efficient photocatalytic synthesis of xylonic acid. Appl. Catal. B Environ. *316*, 121573. https://doi.org/10.1016/j.apcatb.2022.121573.

16. Yuan, L., Qi, M.-Y., Tang, Z.-R., and Xu, Y.-J. (2021). Coupling strategy for CO_2 valorization integrated with organic synthesis by heterogeneous photocatalysis. Angew. Chem. Int. Ed. *60*, 21150–21172. https://doi.org/10.1002/anie.202101667.

17. Lam, E., Miller, M., Linley, S., Manuel, R.R., Pereira, I.A.C., and Reisner, E. (2023). Comproportionation of CO_2 and cellulose to formate using a floating semiconductor-enzyme photoreforming catalyst. Angew. Chem. Int. Ed. *62*, e202215894. https://doi.org/10.1002/anie.202215894.

18. Lam, E., and Reisner, E. (2021). A TiO_2-Co(terpyridine)$_2$ photocatalyst for the selective oxidation of cellulose to formate coupled to the reduction of CO_2 to syngas.

Angew. Chem. Int. Ed. *60*, 23306–23312. https://doi.org/10.1002/anie.202108492.

19. Liu, Z., Ma, J., Hong, M., and Sun, R. (2023). Potassium and sulfur dual sites on highly crystalline carbon nitride for photocatalytic biorefinery and CO_2 reduction. ACS Catal. *13*, 2106–2117. https://doi.org/10.1021/acscatal.2c05661.

20. Qiu, C., Wang, S., Zuo, J., and Zhang, B. (2022). Photocatalytic CO_2 reduction coupled with alcohol oxidation over porous carbon nitride. Catalysts *12*, 672. https://doi.org/10.3390/catal12060672.

21. Huang, C., Wen, Y., Ma, J., Dong, D., Shen, Y., Liu, S., Ma, H., and Zhang, Y. (2021). Unraveling fundamental active units in carbon nitride for photocatalytic oxidation reactions. Nat. Commun. *12*, 320. https://doi.org/10.1038/s41467-020-20521-5.

22. Tian, B., Ho, D., Qin, J., Hu, J., Chen, Z., Voiry, D., Wang, Q., and Zeng, Z. (2023). Framework structure engineering of polymeric carbon nitrides and its recent applications. Prog. Mater. Sci. *133*, 101056. https://doi.org/10.1016/j.pmatsci.2022.101056.

23. Tang, C., Cheng, M., Lai, C., Li, L., Yang, X., Du, L., Zhang, G., Wang, G., and Yang, L. (2023). Recent progress in the applications of non-metal modified graphitic carbon nitride in photocatalysis. Coord. Chem. Rev. *474*, 214846. https://doi.org/10.1016/j.ccr.2022.214846.

24. Zheng, Y., Ruan, Q., Ren, J., Guo, X., Zhou, Y., Zhou, B., Xu, Q., Fu, Q., Wang, S., and Huang, Y. (2023). Plasma- assisted liquid-based growth of g-C_3N_4/Mn_2O_3 p-n heterojunction with tunable valence band for photoelectrochemical application. Appl. Catal. B Environ. *323*, 122170. https://doi.org/10.1016/j.apcatb.2022.122170.

25. Li, D., Wen, C., Huang, J., Zhong, J., Chen, P., Liu, H., Wang, Z., Liu, Y., Lv, W., and Liu, G. (2022). High-efficiency ultrathin porous phosphorus-doped graphitic carbon nitride nanosheet photocatalyst for energy production and environmental remediation. Appl. Catal. B Environ. *307*, 121099. https://doi.org/10.1016/j.apcatb.2022.121099.

26. Zhang, X., Ma, P., Wang, C., Gan, L., Chen, X., Zhang, P., Wang, Y., Li, H., Wang, L., Zhou, X., and Zheng, K. (2022). Unraveling the dual defect sites in graphite carbon nitride for ultra-high photocatalytic H_2O_2 evolution. Energy Environ. Sci. *15*, 830–842. https://doi.org/10.1039/D1EE02369A.

27. Wang, W., Du, L., Xia, R., Liang, R., Zhou, T., Lee, H.K., Yan, Z., Luo, H., Shang, C., Phillips, D.L., and Guo, Z. (2023). In situ protonated-phosphorus interstitial doping induces long-lived shallow charge trapping in porous C_3-$_x$$N_4$ photocatalysts for highly efficient H_2 generation. Energy Environ. Sci. *16*, 460–472. https://doi.org/10.1039/D2EE02680E.

28. Liu, K., Ma, J., Yang, X., Liu, Z., Li, X., Zhang, J., Cui, R., and Sun, R. (2022). Phosphorus/oxygen co-doping in hollow-tube-shaped carbon nitride for efficient simultaneous visible-light-driven water splitting and biorefinery. Chem. Eng. J. *437*, 135232. https://doi.org/10.1016/j.cej.2022.135232.

29. Zhao, D., Wang, Y., Dong, C.-L., Huang, Y.-C., Chen, J., Xue, F., Shen, S., and Guo, L. (2021). Boron-doped nitrogen-deficient carbon nitride-based Z-scheme heterostructures for photocatalytic overall water splitting. Nat. Energy *6*, 388–397. https://doi.org/10.1038/s41560-021-00795-9.

30. Chen, L., Chen, C., Yang, Z., Li, S., Chu, C., and Chen, B. (2021). Simultaneously tuning band structure and oxygen reduction pathway toward high-efficient photocatalytic hydrogen peroxide production using cyano-rich graphitic carbon nitride. Adv. Funct. Mater. *31*, 2105731. https://doi.org/10.1002/adfm.202105731.

31. Babu Ganganboina, A., Dung Nguyen, M., Hien Luong Nguyen, T., Prasetyo Kuncoro, E., and Doong, R.-A. (2021). Boron and phosphorus co-doped one-dimensional graphitic carbon nitride for enhanced visible-light-driven photodegradation of diclofenac. Chem. Eng. J. *425*, 131520. https://doi.org/10.1016/j.cej.2021.131520.

32. Wu, Y., Xiong, P., Wu, J., Huang, Z., Sun, J., Liu, Q., Cheng, X., Yang, J., Zhu, J., and Zhou, Y. (2021). Band engineering and morphology control of oxygen-incorporated graphitic carbon nitride porous nanosheets for highly efficient photocatalytic hydrogen evolution. Nano-Micro Lett. *13*, 48. https://doi.org/10.1007/s40820-020-00571-6.

33. Du, L., Tian, Q., Zheng, X., Guo, W., Liu, W., Zhou, Y., Shi, F., and Xu, Q. (2022). Supercritical CO_2-tailored 2D oxygen-doped amorphous carbon nitride for enhanced photocatalytic activity. Energy Environ. Mater. *5*, 912–917. https://doi.org/10.1002/eem2.12209.

34. Mishra, A., Mehta, A., Basu, S., Shetti, N.P., Reddy, K.R., and Aminabhavi, T.M. (2019). Graphitic carbon nitride (g-C_3N_4)-based metal-free photocatalysts for water splitting: A review. Carbon *149*, 693–721. https://doi.org/10.1016/j.carbon.2019.04.104.

35. Zhang, Y., Chen, Z., Li, J., Lu, Z., and Wang, X. (2021). Self-assembled synthesis of oxygen-doped g-C_3N_4 nanotubes in enhancement of visible-light photocatalytic hydrogen. J. Energy Chem. *54*, 36–44. https://doi.org/10.1016/j.jechem.2020.05.043.

36. Xu, Y., He, X., Zhong, H., Singh, D.J., Zhang, L., and Wang, R. (2019). Solid salt confinement effect: An effective strategy to fabricate high crystalline polymer carbon nitride for enhanced photocatalytic hydrogen evolution. Appl. Catal. B Environ. *246*, 349–355. https://doi.org/10.1016/j.apcatb.2019.01.069.

37. An, S., Zhang, G., Li, K., Huang, Z., Wang, X., Guo, Y., Hou, J., Song, C., and Guo, X. (2021). Self-supporting 3D carbon nitride with tunable n→π* electronic transition for enhanced solar hydrogen production. Adv. Mater. *33*, 2104361. https://doi.org/10.1002/adma.202104361.

38. Zhai, Z., Zhang, H., Niu, F., Liu, P., Zhang, J., and Lu, H. (2022). Mesoporous carbon nitride with π-electron-rich domains and polarizable hydroxyls fabricated via solution thermal shock for visible-light photocatalysis. ACS Nano *16*, 21002–21012. https://doi.org/10.1021/acsnano.2c08643.

39. Shang, Y., Wang, Y., Lv, C., Jing, F., Liu, T., Li, W., Liu, S., and Chen, G. (2022). A broom-like tube-in-tube bundle O-doped graphitic carbon nitride nanoreactor that promotes photocatalytic hydrogen evolution. Chem. Eng. J. *431*, 133898. https://doi.org/10.1016/j.cej.2021.133898.

40. Wang, Q., Xiao, M., Peng, Z., Zhang, C., Du, X., Wang, Z., and Wang, W. (2022). Visible LED photocatalysis combined with ultrafiltration driven by metal-free oxygen-doped graphitic carbon nitride for sulfamethazine degradation. J. Hazard Mater. *439*, 129632. https://doi.org/10.1016/j.jhazmat.2022.129632.

41. Zhai, B., Li, H., Gao, G., Wang, Y., Niu, P., Wang, S., and Li, L. (2022). A crystalline carbon nitride based near-infrared active photocatalyst. Adv. Funct. Mater. *32*, 2207375. https://doi.org/10.1002/adfm.202207375.

42. Li, Q., Zhang, L., Liu, J., Zhou, J., Jiao, Y., Xiao, X., Zhao, C., Zhou, Y., Ye, S., Jiang, B., and Liu, J. (2021). Porous carbon nitride thin strip: Precise carbon doping regulating delocalized π-electron induces elevated photocatalytic hydrogen evolution. Small *17*, 2006622. https://doi.org/10.1002/smll.202006622.

43. Yu, Z., Yue, X., Fan, J., and Xiang, Q. (2022). Crystalline intramolecular ternary carbon nitride homojunction for photocatalytic hydrogen evolution. ACS Catal. *12*, 6345–6358. https://doi.org/10.1021/acscatal.2c01563.

44. Zhang, P., Tong, Y., Liu, Y., Vequizo, J.J.M., Sun, H., Yang, C., Yamakata, A., Fan, F., Lin, W., Wang, X., and Choi, W. (2020). Heteroatom dopants promote two-electron O_2 reduction for photocatalytic production of H_2O_2 on polymeric carbon nitride. Angew. Chem. Int. Ed. *59*, 16209–16217. https://doi.org/10.1002/anie.202006747.

45. Xu, Y., Fan, M., Yang, W., Xiao, Y., Zeng, L., Wu, X., Xu, Q., Su, C., and He, Q. (2021). Homogeneous carbon/potassium-incorporation strategy for synthesizing red polymeric carbon nitride capable of near-infrared photocatalytic H_2 production. Adv. Mater. *33*, 2101455. https://doi.org/10.1002/adma.202101455.

46. Liu, Q., Cheng, H., Chen, T., Lo, T.W.B., Ma, J., Ling, A., and Wang, F. (2021). Boosted CO desorption behaviors induced by spatial dyadic heterostructure in polymeric carbon nitride for efficient photocatalytic CO_2 conversion. Appl. Catal. B Environ. *295*, 120289. https://doi.org/10.1016/j.apcatb.2021.120289.

47. Hu, J., Yang, T., Yang, X., Qu, J., Cai, Y., and Li, C.M. (2022). Highly selective and efficient solar-light-driven CO_2 conversion with an ambient-stable 2D/2D Co_2P@BP/g-C_3N_4 heterojunction. Small *18*, 2105376. https://doi.org/10.1002/smll.202105376.

48. Dong, G., Huang, X., and Bi, Y. (2022). Anchoring black phosphorus quantum dots on Fe-doped $W_{18}O_{49}$ nanowires for efficient photocatalytic nitrogen fixation. Angew. Chem. Int. Ed. *61*, e202204271. https://doi.org/10.1002/anie.202204271.

49. Ruan, X., Cui, X., Cui, Y., Fan, X., Li, Z., Xie, T., Ba, K., Jia, G., Zhang, H., Zhang, L., et al. (2022). Favorable energy band alignment of TiO_2 anatase/rutile heterophase homojunctions yields photocatalytic hydrogen evolution with quantum efficiency exceeding 45.6. Adv. Energy Mater. *12*, 2200298. https://doi.org/10.1002/aenm.202200298.

50. Huang, Z.-F., Song, J., Pan, L., Wang, Z., Zhang, X., Zou, J.-J., Mi, W., Zhang, X., and Wang, L. (2015). Carbon nitride with simultaneous porous network and O-doping for efficient solar-energy-driven hydrogen evolution. Nano Energy *12*, 646–656. https://doi.org/10.1016/j.nanoen.2015.01.043.

51. Wang, X., Meng, J., Zhang, X., Liu, Y., Ren, M., Yang, Y., and Guo, Y. (2021). Controllable approach to carbon-deficient and oxygen-doped graphitic carbon nitride: robust photocatalyst against recalcitrant organic pollutants and the mechanism insight. Adv. Funct. Mater. *31*, 2010763. https://doi.org/10.1002/adfm.202010763.

52. Liu, K., Ma, J., Yang, X., Jin, D., Li, Y., Jiao, G., Yao, S., Sun, S., and Sun, R. (2022). Boosting electron kinetics of anatase TiO_2 with carbon nanosheet for efficient photo-reforming of xylose into biomass-derived organic acids. J. Alloys Compd. *906*, 164276. https://doi.org/10.1016/j.jallcom.2022.164276.

53. Liu, Q., Wei, L., Xi, Q., Lei, Y., and Wang, F. (2020). Edge functionalization of terminal amino group in carbon nitride by in-situ C-N coupling for photoreforming of biomass into H_2. Chem. Eng. J. *383*, 123792. https://doi.org/10.1016/j.cej.2019.123792.

54. Das, R., Das, R., Jena, M., Janka, J., Mishra, S., Jasil, M., Vinod, C.P., Singh, A.K., and Peter, S.C. (2022). Noble-metal-free heterojunction photocatalyst for selective CO_2 reduction to methane upon induced strain relaxation. ACS Catal. *66*, 687–693. https://doi.org/10.1021/acscatal.1c04587.

55. Zhang, J., Liu, K., Sun, S., Sun, R., and Ma, J. (2022). Photo-splitting xylose and xylan to xylonic acid and carbon monoxide. Green Chem. *24*, 8367–8376. https://doi.org/10.1039/D2GC02909J.

56. Ma, J., Li, Y., Jin, D., Yang, X., Jiao, G., Liu, K., Sun, S., Zhou, J., and Sun, R. (2021). Reasonable regulation of carbon/nitride ratio in carbon nitride for efficient photocatalytic reforming of biomass-derived feedstocks to lactic acid. Appl. Catal. B Environ. *299*, 120698. https://doi.org/10.1016/j.apcatb.2021.120698.

57. Yang, X., Ma, J., Sun, S., Liu, Z., and Sun, R. (2022). K/O co-doping and introduction of cyano groups in polymeric carbon nitride towards efficient simultaneous solar photocatalytic water splitting and biorefineries. Green Chem. *24*, 2104–2113. https://doi.org/10.1039/D1GC04323D.

58. Tan, J., Li, Z., Li, J., Meng, Y., Yao, X., Wang, Y., Lu, Y., and Zhang, T. (2022). Visible-light-assisted peroxymonosulfate activation by metal-free bifunctional oxygen-doped graphitic carbon nitride for enhanced degradation of imidacloprid: Role of non-photochemical and photocatalytic activation pathway. J. Hazard Mater. *423*, 127048. https://doi.org/10.1016/j.jhazmat.2021.127048.

59. Sun, X., Sun, L., Li, G., Tuo, Y., Ye, C., Yang, J., Low, J., Yu, X., Bitter, J.H., Lei, Y., et al. (2022). Phosphorus tailors the *d*-band Center of copper atomic sites for efficient CO_2 photoreduction under visible-light irradiation. Angew. Chem. Int. Ed. *61*, e202207677. https://doi.org/10.1002/anie.202207677.

60. Zhang, Y., Luo, H., Kong, L., Zhao, X., Miao, G., Zhu, L., Li, S., and Sun, Y. (2020). Highly efficient production of lactic acid from xylose using Sn-beta catalysts. Green Chem. *22*, 7333–7336. https://doi.org/10.1039/D0GC02596H.

61. Wang, M., Liu, M., Lu, J., and Wang, F. (2020). Photo splitting of bio-polyols and sugars to methanol and syngas. Nat. Commun. *11*, 1083. https://doi.org/10.1038/s41467-020-14915-8.

62. Zhou, H., Wang, M., and Wang, F. (2022). Oxygen-controlled photo-reforming of biopolyols to CO over Z-scheme CdS@g-C_3N_4. Chem *8*, 465–479. https://doi.org/10.1016/j.chempr.2021.10.021.

STAR★METHODS

KEY RESOURCES TABLE

REAGENT or RESOURCE	SOURCE	IDENTIFIER
Chemicals, peptides, and recombinant proteins		
Melamine	Shanghai Macklin Biochemical Technology Co., Ltd	CAS: 108-78-1
Ammonium fluoride	Shanghai Aladdin Biochemical Technology Co., Ltd.	CAS: 12125-01-8
Potassium hydroxide	Shanghai Aladdin Biochemical Technology Co., Ltd.	CAS: 1310-58-3
D-Xylose	Shanghai Aladdin Biochemical Technology Co., Ltd.	CAS: 6763-34-4
Arabinose	Shanghai Aladdin Biochemical Technology Co., Ltd.	CAS: 10323-20-3
Glucose	Shanghai Aladdin Biochemical Technology Co., Ltd.	CAS: 921-60-8
Mannose	Shanghai Aladdin Biochemical Technology Co., Ltd.	CAS: 3458-28-4
L-Rhamnose monohydrate	Shanghai Aladdin Biochemical Technology Co., Ltd.	CAS: 10030-85-0
Fructose	Shanghai Aladdin Biochemical Technology Co., Ltd.	CAS: 7660-25-5
Ethylenediaminetetraacetic acid	Shanghai Aladdin Biochemical Technology Co., Ltd.	CAS: 60-00-4
p-Phthalic acid	Shanghai Aladdin Biochemical Technology Co., Ltd.	CAS: 100-21-0
Lactic acid	Shanghai Aladdin Biochemical Technology Co., Ltd.	CAS: 79-33-4
Formic acid	Sigma-Aldrich (Shanghai) Trading Co., Ltd.	CAS: 64-18-6

RESOURCE AVAILABILITY

Lead contact

Further information and requests for resources and reagents should be directed to and will be fulfilled by the lead contact, Jiliang Ma (jlma@dlpu.edu.cn).

Materials availability

This study did not generate new unique reagents.

Data and code availability

- Data reported in this paper will be shared by the lead contact upon request.
- This paper does not report original code.
- Any additional information required to reanalyze the data reported in this paper is available from the lead contact upon request.

METHOD DETAILS

Preparation of O-CNNTs-x, O-CN, and CN

Initially, 2.0 g of melamine and 25 mL of deionized water were uniformly mixed with a certain mass (0.5 g, 1.0 g, 2.0 or 3.0 g) of ammonium fluoride. The obtained mixture was placed in a 50 mL Teflon-lined autoclave and hydrothermally treated at 180°C for 12 h. After cooling to room temperature, the product was centrifuged (8000 rpm, 5 min), and then dried at 60°C for 8 h. The as-obtained white acicular precursor was heated at 560°C for 4 h in N_2 atmosphere to yield O-CNNTs-x (x = 0.5, 1.0, 2.0, 3.0). O-CN was prepared via the similar steps of O-CNNTs-x without ammonium fluoride. In contrast to O-CN, CN was obtained from the same calcination program without hydrothermal treatment.

Photocatalytic activity tests

An amount of the photocatalyst (e.g. O-CNNTs-x, O-CN, CN), 30 mL of solution (e.g. H_2O, KOH, HCl) and 100 mg of xylose were added in the quartz reaction bottle (50 mL) and treated under ultrasound for 20 min. Prior to irradiation, the reactor was degassed with CO_2 (110 kPa, 99.99%) to remove air for five times. Then,

the reactor was irradiated at 30°C using the Vlight lamp (10 W) to drive the simultaneous photocatalytic biorefinery and CO_2 conversion. The gas product (CO) of the reaction was detected by gas chromatography (GC7900, Timex) equipped with a thermal conductivity detector (TCD) and a flame ionization detector (FID). The liquid product yields (e.g. glyceraldehyde, formic acid, lactic acid, etc.) and the reactants conversion were analyzed by high-performance liquid chromatography (HPLC).

Poisoning experiments and universality tests

Reaction systems containing 10 mg of O-CNNTs-2.0, 100 mg of xylose, 30 mL of 1.0 M KOH solution, and 5 mmol of inhibitors (e.g. PTA, EDTA) were transferred to the quartz reaction bottle (50 mL) and then treated under ultrasound for 20 min. The reactors were sealed, vacuumed and inflated with CO_2 (99.99%) for five times to achieve a CO_2 pressure of 110 kPa. Then, the reaction was typically conducted at 30°C under a 10 W Vlight lamp illumination for 5 h. The obtained samples were evaluated using the same methodology as photocatalytic activity tests.

For universality tests, 10 mg of O-CNNTs-2.0 and 100 mg of the substrate, such as glucose, rhamnose, fructose, mannose, xylose, and arabinose, were dispersed in the quartz reaction bottle (50 mL) containing 30 mL of 1.0 M KOH solution, and then ultrasonicated for 20 min. After evacuation and inflation with CO_2 (110 kPa, 99.99%), the reactors were irradiated by a 10 W Vlight lamp for 5 h at 30°C.

Cyclic experiments

The cycling experiments were conducted under the conditions similar with the poisoning experiments without inhibitors. Following the photocatalytic test, the catalysts were centrifuged, rinsed and dried for reuse. This process was repeated for a total of five tests.

Isotope-labelling testing

The test procedure for the $^{13}CO_2$ isotope experiment was the same as that for the standard photocatalytic biomass refining and CO_2 reduction test, except that $^{12}CO_2$ was replaced with $^{13}CO_2$ and the gas products were analyzed by the gas chromatography-mass spectrometry and C NMR.

Catalyst characterization

Scanning electron microscopy (SEM) images were explored on Hitachis-4800, while transmission electron microscopy (TEM) images were observed using a JEM-2100 CXII. Powder X-ray diffraction (XRD) patterns were acquired using a Bruker D8 Focus diffractometer (Cu-Kα radiation, λ = 0.15418 Å). Brunauer-Emmett-Teller (BET) specific surface areas were obtained from a Micromeritics ASAP 2020 apparatus. Fourier transform infrared (FT-IR) spectrum was collected on a Bruker Tensor 27 spectrophotometer. X-ray photoelectron spectroscopy (XPS) analysis were carried out on a Kratos Axis Ultra DLD spectrometer employing an amonochromated AlKR X-ray source (1486.6 eV). Ultraviolet-visible diffuse reflectance spectrum (UV-vis DRS) was achieved on a Cary 5000 spectrophotometer by using $BaSO_4$ as the reference. Ultraviolet photoelectron spectroscopy (UPS) was obtained from a He I (21.22 eV) as a monochromatic discharge light source and a VG Scienta R4000 analyzer. A sample bias of -5 V was applied to observe the secondary electron cutoff (SEC). The photoluminescence (PL) measurements were obtained using an Edinburgh FLS-920 spectrometer under 350 nm excitation. Electron spin-resonance spectroscopy was obtained from a Bruker JES-FA300 spectrometer with spin-trapped reagent (e.g. 2,2,6,6-tetramethylpiperidine-1-oxyl, 5,5-dimethyl-l-pyrroline N-oxide).

Photoelectrochemical measurements

Photoelectrochemical measurements were carried out on a CHI760E electrochemical workstation with a standard three-electrodes system. Among them, a Pt wire was used as the counter electrode, and the reference electrode was the saturated Ag/AgCl. The cleaned F-doped tin oxide (FTO) glass was used as the working electrode. 5 mg of corresponding photocatalyst and 20.0 μL of Nafion (Sigma Aldrich, 5 wt.%) were added into 980.0 μL of ethanol to form a homogeneous slurry. The homogeneous slurry was ultrasonicated for 30 min and then evenly spread on the FTO glass. The obtained system was dried at 60°C for 1 h. A 0.5 M Na_2SO_4 solution (pH = 6.8) was used as the supporting electrolyte. The incident visible light source was Xe lamp (300 W). The photocurrent-time was investigated in the irradiation of Xe lamp at a bias potential of 0.5 V vs. Ag/AgCl. The electrochemical impedance spectroscopy (EIS) was recorded in the frequency

range from 0.01 Hz to 10 kHz by an AC voltage amplitude of 10 mV. The Mott-Schottky (M-S) plots were carried out by using the frequency of AC potential at 500, 800, and 1000 Hz to evaluate the flat potential.

Products analysis

The liquid products were analyzed by high-performance liquid chromatography (HPLC, Agilent 1260 Infinity II) with a Bio-Rad Aminex HPX-87H column, in which a 5 mM H_2SO_4 aqueous solution was used as mobile phase (flow rate, 0.5 mL min^{-1}). The temperature of column was set at 55°C and the total time to finish the product analysis was set at 30 min. The conversion of biomass monosaccharides and yields of oxidation half-reaction products were calculated as follows:

$$\text{Conversion (\%)} = \frac{\text{Moles of carbon in feedstock consumed}}{\text{Moles of carbon in feedstock input}} \times 100\%$$

$$\text{Product yield (\%)} = \frac{\text{Moles of carbon in organic acid}}{\text{Moles of carbon in feedstock input}} \times 100\%$$

The production of CO was quantified through headspace gas analysis (1.0 mL) by gas chromatography (GC-7900) equipped with thermal conductivity detector (TCD) and flame ionized detectors (FID), and ultrapure argon was used as the carrier gas.

QUANTIFICATION AND STATISTICAL ANALYSIS

Figures were analyzed by Origin from the raw data.